# Calibrating a nanoindenter for very shallow depth indentation using equivalent contact radius

Damir R Tadjiev, Russell J Hand, Simon A Hayes


# Calibrating a nanoindenter for very shallow depth indentation using equivalent contact radius

| | |
|---|---|
| Journal: | *Philosophical Magazine & Philosophical Magazine Letters* |
| Manuscript ID: | TPHM-09-Jul-0315.R2 |
| Journal Selection: | Philosophical Magazine |
| Date Submitted by the Author: | 13-Nov-2009 |
| Complete List of Authors: | Tadjiev, Damir; University of Sheffield, Engineering Materials<br>Hand, Russell; University of Sheffield, Engineering Materials<br>Hayes, Simon; University of Sheffield, Engineering Materials |
| Keywords: | nanoindentation, mechanical properties |
| Keywords (user supplied): | tip area function, calibration, shallow depths |
| | |

# Calibrating a nanoindenter for very shallow depth indentation using equivalent contact radius

Damir R. Tadjiev, Russell J. Hand† and Simon A. Hayes

*Department of Engineering Materials, University of Sheffield, Sheffield, UK*

Mappin Street, Sheffield S1 3JD, UK

*(Received 21 July 2009; final version received 2009)*

Nanoindenter tips are usually modeled as axisymmetric cones, with calibration involving finding a fitting function relating the contact area to the contact depth. For accurate calibration of shallow depth indentation this is not ideal because it means that deeper indents tend to dominate the fitting function. For an axisymmetric object it is always possible to define an equivalent contact radius (which in the case of nanoindentation is linearly related to the reduced modulus) and to obtain a fitting function relating this equivalent contact radius to indentation depth. The equivalent contact radius approach is used here to provide shallow depth calibration of a nanoindenter tip at three separate times. The advantage of the equivalent contact radius methodology is that it provides a clearer physical interpretation of the changes in tip shape than a conventional area based fit. We also show that the minimum depth for a reliable hardness measurement is obtainable increases as the tip blunts with age but that consistent measurements of very near surface elastic moduli can be made if the blunting of the tip over time is fully accounted for in the tip area function calibration.

Keywords: tip area function, calibration, nanoindentation, shallow depths



† Corresponding author. Tel.: +44 (0)114 2225465. Email address: r.hand@shef.ac.uk (R.J. Hand).

## 1. Introduction

Nanoindentation differs from conventional indentation in that the results are based not on imaging of the residual indent (which would be very challenging, and largely impracticable, for very low load indents), but rather on a calibrated tip area function (TAF) which describes the variation of the contact area ($A_c$) of the tip as a function of contact depth ($h_c$). In the ideal case the indenter has a simple axisymmetric shape and, hence, the TAF can be described by a simple mathematical function. Thus even the commonly used Berkovich indenter, which is actually a triangular pyramid, is usually modelled by an equivalent axisymmetric cone, as assumed in the conventional Oliver and Pharr (O&P) approach.

In actuality any real tip shape will deviate from its ideal geometry to some greater or lesser extent, even when new, and this will become more marked as the tip becomes worn over time due to its use in indentation [1] and, commonly, secondary use in imaging the residual indent [2]. Thus an equivalent cone model of a Berkovich tip will break down at some point [3, 4] and one approach to this problem is to treat the very near tip region using a Hertzian analysis (see, for example, [5]); clearly this still treats the tip as an axisymmetric object.

In the commonly adopted Oliver and Pharr approach TAF calibration is carried out by indenting a material of known modulus, which is assumed to have i) an elastic modulus that is unvarying with depth and ii) a low $E/H$ value which means that there will be minimum pile-up and sink-in [6]. The stiffness, $S$, of the combined indenter/ indented materials system is then assessed from the initial (elastic) part of the unloading curve and the area of the indentation is then obtained using

$$A = \frac{\pi S^2}{4\beta^2 E_r^2} \qquad (1)$$

where $\beta$ is a geometric correction factor (in this work taken to be equal to 1.05) [6] and $E_r$ is the reduced modulus, which accounts for the fact that the measured displacement includes contributions from the sample and the indenter. $E_r$ is given by

$$\frac{1}{E_r} = \frac{1-\nu^2}{E} + \frac{1-\nu_i^2}{E_i} \qquad (2)$$

where $E$, $E_i$ and $\nu$, $\nu_i$ are the elastic moduli and Poisson's ratios of sample and the indenter respectively. For the diamond Berkovich indenter $E_i$ = 1141 GPa and $\nu_i$ = 0.07, and for fused silica (which largely obeys the two assumptions mentioned above) used as a standard in this work $E$ = 72 GPa and $\nu$ = 0.17, respectively; hence $E_r$ is equal to 69.6 GPa. The TAF is then obtained by fitting $A$ as a function of the contact depth, $h_c$.

The work described here forms part of a larger project to examine the mechanical properties of the surface hydration layers formed on silicate glasses [7, 8]. This requires reliable calibration of TAFs for shallow (we have been focusing on less than 80 nm indentation) depths. Calibration of the TAF for shallow depths is a particular problem for a number of reasons: imaging is most difficult in this region (and at the lowest loads impossible due to the occurrence of purely elastic behaviour); and although the data are more sensitive to random errors in this region (*i.e.* they are noisier) the data obtained at larger depths tend to have larger absolute (as distinct from relative) residuals. The latter point means that any large depth data tend to dominate the curve fitting thereby reducing the accuracy of any fit at shallow depth. Conventionally this issue is addressed by providing different fits over different depth

ranges but an alternative method is to select an appropriate data transform [9]. Here it has been therefore decided to fit

$$r_c = \sqrt{A/\pi} \qquad (3)$$

as a function of $h_c$, where $r_c$ is the contact radius of the equivalent axisymmetric body. This has the advantage of giving an equal distribution of residuals due to the approximately linear scaling between $r_c$ and $h_c$ that can be reasonably expected for all tip geometries. Also combining equations (1) and (3) gives

$$r_c = \frac{S}{2\beta E_r} \qquad (4)$$

*i.e.* $E_r \propto 1/r_c$ meaning that the calibration is based entirely on a linear relationship rather than a quadratic one.

## 2. Experimental procedure

### *2.1 Instrumentation and reference material*

A commercial Hysitron Triboscope® nanoindenter (Hysitron Inc., USA) mounted on a Dimension 3100 (Veeco Digital Instruments) nanoscope equipped with a Berkovich tip (Hysitron, original tip radius 150 nm) was used. The indenting system is housed in under a thermal and acoustic isolation hood which is mounted on a vibration resistant table. The nanoindenter has load and displacement resolution of 1 μN and 0.1 nm, respectively. Calibration was undertaken by making indentations on standard fused silica samples to obtain data for contact depth in the range of 0-100 nm. The first tip area function (TAF1) was calibrated on 10 × 10 × 3 mm fused silica sample that came with nanoindenter and had surface roughness, $R_a$, of 0.69 nm, while the second and the third (TAF2 and TAF3) tip area functions were calibrated on new 40 × 25 × 3 mm fused silica slides (Heraeus, $R_a$ = 0.54 nm). 3 data sets were collected at

approximately 1 year time intervals (see table 1). All experiments were carried out in a quasi-static mode and during each calibration run multiple arrays of 8 × 8 indents spaced 4 μm apart on both the *x* and *y* axes were made, with each indent providing a single measurement of stiffness and load. A standard loading scheme of 5 s up-load, 5 s dwell and 5 s unloading was used. All measurements were carried out at room temperature (24±1°C) and a relative humidity of 60-80% with drift correction on. The indenter is continuously powered so that the electronics are maintained in a stable state. Drift was measured by running 0.1 μN test with a 20 s hold at peak load and measuring displacement drift during this hold. The remainder of the test was corrected by the measured drift rate the typical value of which did not exceed 0.1 nm/s. Approximately 1000 data points were collected for each calibration data set with an emphasis on low load indentation values.

Prior to the measurements, the compliance of the indenter column (machine compliance) was measured by making at least 25 high-load indentations (5000 to 10000 μN) on fused silica and then plotting compliance (inverse stiffness) versus *1/P* (where *P* is applied load) for the obtained data. Reliability of the determined compliance value was checked by plotting load over stiffness squared ($P/S^2$) versus contact depth and making sure that the slope of the curve is 0. This approach was originally proposed by Oliver and Pharr [6] for the measurements at high-load indentations, but it has been found in this work that it also works well at low-load indentations.

Prior to each test the fused silica samples were cleaned by rinsing in pure ethanol and drying using a warm air blower. The surface region to be indented was then imaged using the instrument in the scanning probe microscope (SPM) mode to ensure that the surface was free of dirt and contamination.

### *2.2 Data analysis and TAF fitting*

Following the standard O&P method [10] the initial unloading contact stiffness, $S$, was obtained from the slope of a power law fit to the initial part of the unloading curves using the installed Hysitron software. The power law used was

$$P = \alpha\left(h - h_f\right)^m \qquad (5)$$

where $P$ is load, $h$ is the measured indention depth, $h_f$ is the residual indentation depth after removal of the indenter and $\alpha$ and $m$ are fitting constants. The unloading stiffness ($S = \mathrm{d}P/\mathrm{d}h$) was then obtained by differentiation and equations (1) were used to obtain the equivalent axisymmetric contact radius.

Contact depth $h_c$ was calculated by the Hysitron indenter software using

$$h_c = h_{\max} - 0.75\frac{S}{P_{\max}} \qquad (6)$$

where $h_{\max}$ and $P_{\max}$ are, respectively, the maximum depth and load during the indentation [8].

## 3. Results and discussion

Figure 1 shows a plot of $r_c$ versus $h_c$ for the tip when new. In this case a linear fit was found to be applicable and a linear regression fit to the data shown gave

$$r_c = 2.899h_c + 23.5 \qquad (7)$$

with an $r^2$ value of 0.990. It is interesting to note that Thurn and Cook [11] proposed a three term area function, which actually involves only two independent parameters, to calibrate the TAF. They took a harmonic average of a spherical tip profile (with radius $R$) and a perfect conical shape (with included angle 2α) and obtained

$$A = \frac{\pi}{\cot^2\alpha}h_c^2 + 4R\pi h_c + 4R^2\pi\cot^2\alpha \qquad (8)$$

Combining equations (3) and (8) gives

$$r_c = \frac{h_c}{\cot\alpha} + 2R\cot\alpha \qquad (9)$$

*i.e.* a straight line as seen in figure (1a). The original derivation of equation (8) involved use of the binomial expansion which requires that the contact radius $a > 2R\cot\alpha$, and implies that there is a flat end, the radius of which corresponds to the constant term in equation (8), even though the original harmonic average does not assume this. Using equation (9) for the data shown in figure 1 gives an included angle $\alpha = 70.9^{o} \pm 0.3^{o}$ and $R = 33.9 \pm 1.2$ nm indicating that the original tip conformed reasonably closely to the expected equivalent cone angle of 70.32° (see, for example, [12]). However, as noted above, equation (9) in fact indicates that there is a flat right at the tip. In the current case the radius of this flat is $r_c = 23.5 \pm 0.9$ nm.

For comparative purposes a 9 term Oliver and Pharr TAF fit was also undertaken (see figure 1b). This gave

$$A = 23.399h_c^2 + 604.968h_c + 8.694h_c^{1/2} + 6.444\times10^{-5}h_c^{1/4} + 1.619h_c^{1/8} + 30.070h_c^{1/16} + 1.773\times10^{-8}h_c^{1/32} + 31.478h_c^{1/64} + 41.720h_c^{1/128} \qquad (10)$$

with an $r^2$ value of 0.988.

Figure 2a shows a later calibration on the same tip carried out after it had received significant usage. The fact that the regression line from the first calibration can be displaced upwards to overlay the data from the second calibration shows that although the very near tip region has indeed become blunter away from this region the tip is essentially unmodified. This fact cannot be simply inferred from a conventional TAF plot (figure 2b). It would also appear that although the tip shape has been modified that the effective radius of the flat right at the tip has remained essentially unchanged as dataset 2 intercepts the *y*-axis at essentially the same point as dataset 1.

The exact displacement between the two curves was evaluated by ensuring that the residuals in the straight line portion were equally scattered about zero by examining the moving average. The moving average was also used to identify an appropriate break point below which an alternative curve fit was required. Empirically it was found that using a function based on that proposed by Oliver and Pharr for the tip area fit was most effective for this regime (see figure 3). The fitting was carried out using the non-linear regression routines supplied in SigmaPlot 10 (Systat). Thus for the particular dataset shown in figures 2 and 3 the resultant fit was

$$\begin{aligned} r_c &= 2.0115h_c + 12.1929h_c^{1/2} + 19.7669 \qquad h_c < 48\,\text{nm} \\ r_c &= 2.8969h_c + 61.67 \qquad\qquad\qquad\quad h_c \geq 48\,\text{nm} \end{aligned} \tag{11}$$

In this case the overall $r^2$ value for the fit was 0.999. The improved $r^2$ value for this fit compared to the original fit is due to a smaller spread in the initial data, which is due to the use of a calibration piece of silica with lower surface roughness. Although a split function approach could also be used for the TAF fit it is much less obvious as to where to split the fitting function. Thus the equivalent radius approach potentially offers some benefit in determining an appropriate fit.

Similar features were found with a third calibration carried out at a later date (see figure 4). Again at the greater depths the calibration data appeared to be simply displaced with respect to the original calibration but in the very near tip region the detailed shape had further changed and once again an empirical fit was used in this region. In this case the combined fit was

$$\begin{aligned} r_c &= 2.5050h_c + 6.1533h_c^{1/2} + 44.9516 \qquad h_c < 55\,\text{nm} \\ r_c &= 2.8969h_c + 68.94 \qquad\qquad\qquad\quad h_c \geq 55\,\text{nm} \end{aligned} \tag{12}$$

It can be seen that the fit is slightly less good right at the increasingly blunt indenter tip but additional terms gave no benefit in terms of quality of fit. The overall $r^2$ value for the fit is 0.998. As well as showing how the tip geometry is being blunted over

time the results in figure (4a) once again emphasize how the stiffness of the indentation system is affected by the tip geometry especially at low loads ($r_c$ is directly proportional to $S$; see equation 4).

The residuals for all 3 calibrations are shown in figure (5a). It can be clearly seen that they are in general uniformly distributed about zero indicating both a good fit and that, as desired, all points have essentially been equally weighted in obtaining the fit. As noted above it can be seen that the spread of data in the first fit seen in figure (5) is wider (reflected in the poorer $r^2$ value for this fit) and there is an asymmetry in the residuals in the very near tip region for the third calibration indicating a relatively poor fit in this region. Figure (5b) shows the corresponding residuals for the Oliver and Pharr fit having re-expressed everything in terms of equivalent radius for comparative purposes. It can be seen that the distribution of the residuals is very similar, except in the region corresponding to the flat in the original calibration run. Thus the two methodologies overall provide similar levels of accuracy the real advantage of the methodology proposed here is that it directly provides a clearer physical picture of progressive changes in indenter tip geometry.

As a further check equations (7), (10) and (11) were substituted in equation (4) and the reduced modulus was recalculated for the three data sets and the results are shown in figure (6a). In all cases the data are essentially scattered around the expected value of 69.6 MPa. Figure (6a) also indicates that consistent measurements of very near surface elastic moduli can be made if the blunting of the tip over time is fully accounted for in the tip calibration.

It is obvious that the surface contamination and hydration may compromise the accuracy of shallow depth indentations. As outlined above cleaning and SPM was used to ensure that the indented region was clean prior to indentation. Also as figure

(5a) shows that the residuals are essentially equally distributed across the entire data range there is no evidence of any cleaning of contamination during successive indents. Hydration is more of a problem. Hydration layer depths of 5 nm to 10 nm [7, 15] have previously been suggested for pure silica. Fundamentally this is an issue for any shallow depth calibration of a nanoindenter in that all calibration techniques assume that there is no variation of modulus with depth whereas a hydrated layer would be expected to result in a reduction in modulus as the surface is approached. In this case one would expect to see an apparent decrease in equivalent contact radius (i.e. an apparent sharpening of the tip) due to the over-estimation of the value of $E_r$ used in equation (4). The fact that we do not observe this behaviour, rather the opposite over time, suggests that for the silica sample examined here hydration is not a significant problem although its presence cannot be absolutely ruled out. The fact that the noise increases at the very shallowest of depths is, we believe, an inevitable consequence of the fact that the measured quantities are particularly small in this region and thus the signal to noise ratio is reduced.

For nanoindentation hardness is defined as

$$H = \frac{P_{\max}}{A} = \frac{P_{\max}}{\pi r_c^2} \qquad (12)$$

where $P_{\max}$ is the maximum load during the indentation. Hardnesses calculated in this fashion are shown in figure (6b). In all cases it can be seen that the measured hardness tends to decrease in the very near surface region. Unfortunately the greater amount of noise present in the original calibration 1 data makes it difficult to identify a clear trend in behaviour, although at very low depths there is an apparent decrease in hardness with decreasing indentation depth; a clearer decrease in hardness with decreasing indentation depth is apparent for the other two datasets and the minimum indentation depth required for meaningful hardness measurements appears to increase

as the tip becomes increasingly blunt. At depths greater than the minimum indentation depth for meaningful hardness measurements no indentation size effect is observed, which is in agreement with the results obtained by other researchers [3, 10, 13, 14]. The apparent decrease in hardness with decreasing depth very near the surface arises because in fact fully elastic deformation is occurring in this region and thus hardness is not actually a meaningful measurement in this region. The reduced elastic moduli (over the entire measured depth range) and hardness values (for indentation depths >15nm) obtained with the three different calibrations are compared in Table 1.

Reduced moduli and hardness values were also calculated using the results of 9 term Oliver and Pharr TAF type fits (see equation (10) for the fit for calibration run 1) and the results are shown in figure 7. Although for calibration runs 2 and 3 the differences between the two fitting techniques are relatively small there is significant difference in the results from calibration run 1 where the Oliver and Pharr fit leads to a significant over-estimation of both reduced modulus and hardness at low depths (compare figures 6 & 7). One might argue that as a single 9 term Oliver and Pharr type fit has been used for all 3 calibration runs whereas for the equivalent contact radius technique for calibration runs 2 and 3 the data were split into 2 parts that we are biasing things against the Oliver and Pharr fit. However the Oliver and Pharr fit produced significant over-estimations of both reduced modulus and hardness at low depths with calibration run 1 where the data were not split for either fitting process. Thus the Oliver and Pharr type fit seems not to capture the initial tip geometry (which is essentially ideal apart from a flat right at the tip) very well, even though once the tip shape is changed through use the Oliver and Pharr fit works well. Overall we suggest that the major advantage of the equivalent contact radius fitting over the Oliver and

Pharr one is that it provides for a simple physical interpretation of the tip geometry and how it is changing with time.

## 5. Conclusions

3 detailed shallow depth calibrations at approximately yearly intervals have been carried out on the same tip. As one would expect there is clear evidence of blunting over time. When the tip was new the equivalent contact radius, which is related to the contact area via equation (3), was linearly related to the contact depth apart from a flat right at the tip thus demonstrating that the tip was geometrically good. The equivalent contact radius approach therefore gives a clear physical interpretation of the tip geometry and dealt with flat at the tip in a better fashion than a 9 term Oliver and Pharr type fit. The equivalent radius approach means that the shallow depth indentation data is automatically weighted equally in the fitting process. As the tip became blunter with use the relationship between equivalent radius and the contact depth starts to deviate from a linear relationship at very low depths but applies at larger depths and still provides a clear physical interpretation of the changes at the tip. Thus, although as good calibrations can be obtained using an Oliver and Pharr type fit, the methodology proposed here provides a clearer physical picture of the tip geometry. It is also worthy of note that $E_r \propto 1/r_c \propto 1/\sqrt{A}$ so it arguably makes more sense to calibrate directly using a linear relationship. Finally we note that consistent measurements of very near surface elastic moduli can be made if the blunting of the tip over time is fully accounted for in the tip calibration.

## Acknowledgements

DT thanks the ORSAS, UK and the University of Sheffield for scholarships enabling him to undertake this work.

## References


[1] Mencik J. Determination of mechanical properties by instrumented indentation. Meccanica 2007; 42: 19.

[2] Hysitron. User's Manual for Tribiscope Nanomechanical Test System NRL-M-015. Minneapolis, USA, 2003: 63.

[3] Doerner MF, Nix WD. A method for interpreting the data from depth-sensing indentation instruments. Journal of Materials Research 1986; 1: 601.

[4] Pethica JB, Hutchings R, Oliver WC. Hardness measurement at penetration depths as small as 20-nm. Philosophical Magazine a-Physics of Condensed Matter Structure Defects and Mechanical Properties 1983; 48: 593.

[5] Gerberich WW, Yu W, Kramer D, Strojny A, Bahr D, Lilleodden E, Nelson J. Elastic loading and elastoplastic unloading from nanometer level indentations for modulus determinations. Journal of Materials Research 1998; 13: 421.

[6] Oliver WC, Pharr GM. Measurement of hardness and elastic modulus by instrumented indentation: Advances in understanding and refinements to methodology. Journal of Materials Research 2004; 19: 3.

[7] Hand RJ, Tadjiev DR, Hayes SA. Nano-indentation and surface hydration of silicate glasses. Journal of the Ceramic Society of Japan 2008; 116: 846.

[8] Tadjiev DR, Hand RJ. Inter-relationships between composition and near surface mechanical properties of silicate glasses. Journal of Non-Crystalline Solids 2008; 354: 5108.

[9] NIST. Engineering Statistics Handbook Section 4.4.5.2. http://www.itl.nist.gov/div898/handbook/pmd/section4/pmd452.htm, accessed 21.7.09.

[10] Oliver WC, Pharr GM. An improved technique for determining hardness and elastic-modulus using load and displacement sensing indentation experiments. Journal of Materials Research 1992; 7: 1564.

[11] Thurn J, Cook RF. Simplified area function for sharp indenter tips in depth-sensing indentation. Journal of Materials Research 2002; 17: 1143.

[12] Hay JL, Pharr GM. Instrumented Indentation Testing. Ohio, USA, 2000: 231.

[13] Gong JH, Miao HZ, Peng ZJ. Analysis of the nanoindentation data measured with a Berkovich indenter for brittle materials: effect of the residual contact stress. Acta Materialia 2004; 52: 785.

[14] Qian LM, Li M, Zhou ZR, Yang H, Shi XY. Comparison of nano-indentation hardness to microhardness. Surface & Coatings Technology 2005;195:264.

[15] Hench L.L. and Clark D.E., Physical chemistry of glass surfaces. J. Non-Cryst. Solids 1978; 28: 83.

Table 1. Summary of mechanical properties (quoted errors are 3 standard deviations).

| Data set | Date | No. of indents | $E_r$ /GPa | $H$ (>15nm) /GPa |
|---|---|---|---|---|
| TAF1 | Aug 2007 | 1540 | 69.1 ± 0.6 | 8.9 ± 0.2 |
| TAF2 | July 2008 | 960 | 69.6 ± 0.3 | 8.8 ± 0.1 |
| TAF3 | May 2009 | 982 | 69.6 ± 0.3 | 8.8 ± 0.1 |

Figure 1. Calibration data obtained when the tip was new.

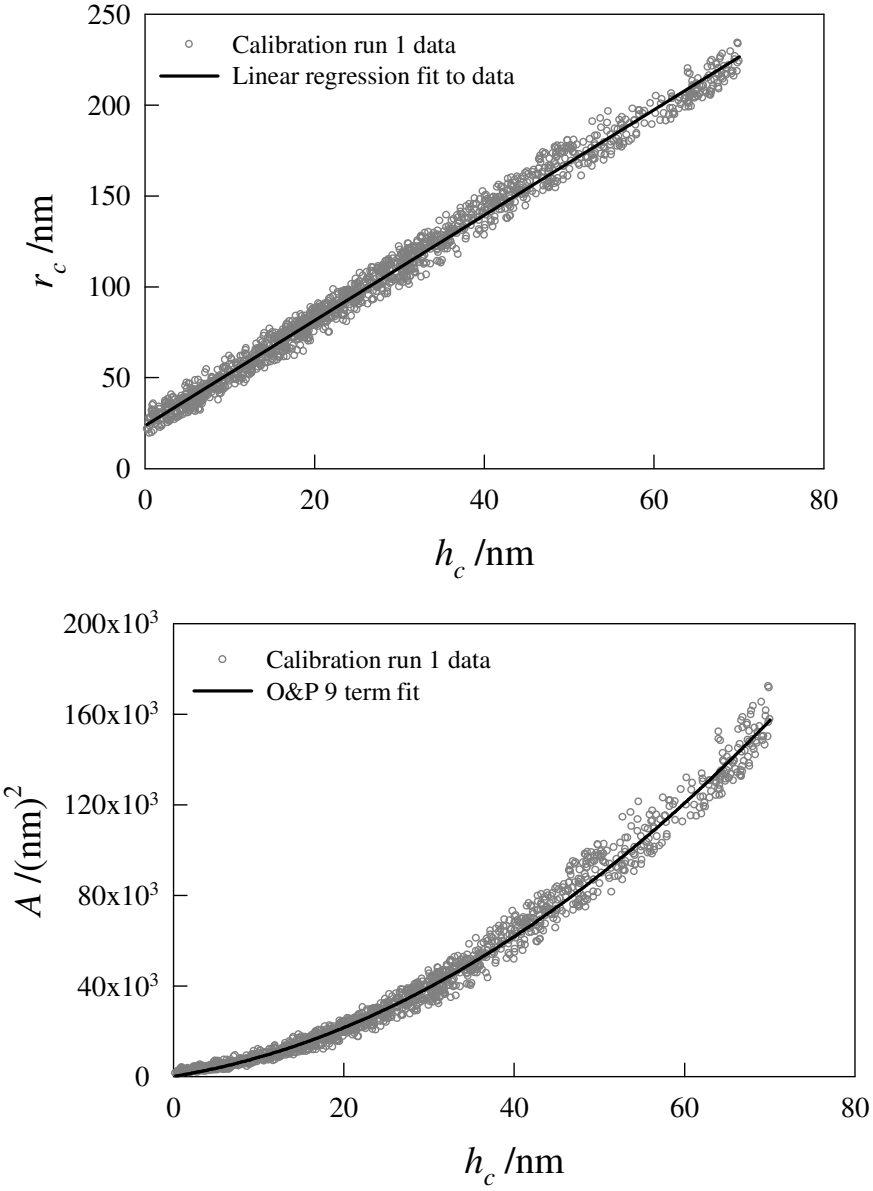

Figure 2. Original calibration data plus data from the second (later) calibration a) plotted as $r_c$ versus $h_c$ and b) plotted as $A$ versus $h_c$.

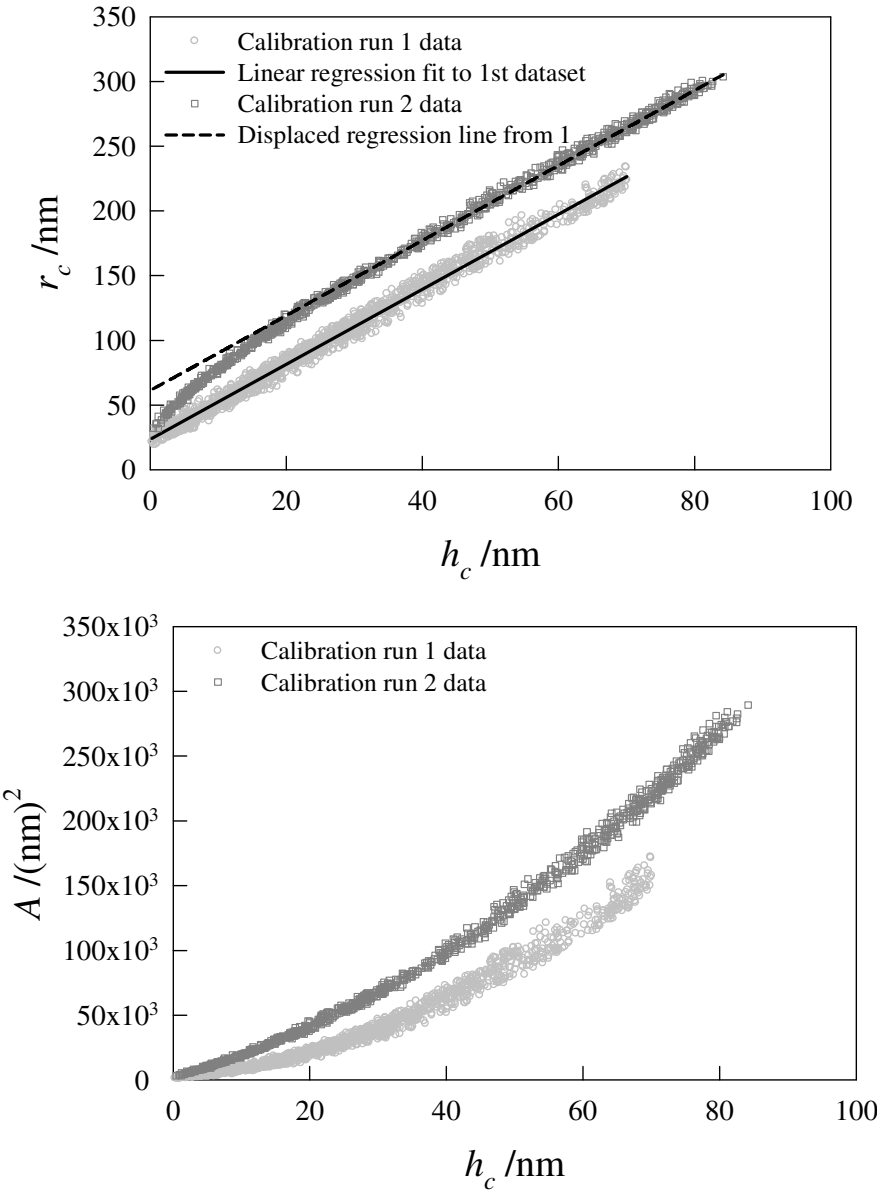

Figure 3. Data from the second calibration showing a) a fit of $r_c = ah_c + bh_c^{1/2} + c$ over the lowest depth region b) the combined fit given by equation (10) over the entire data range.

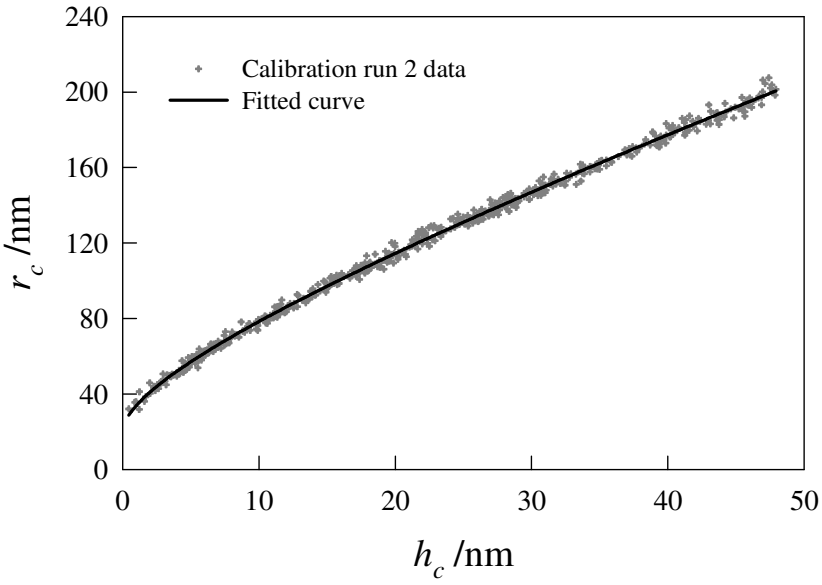


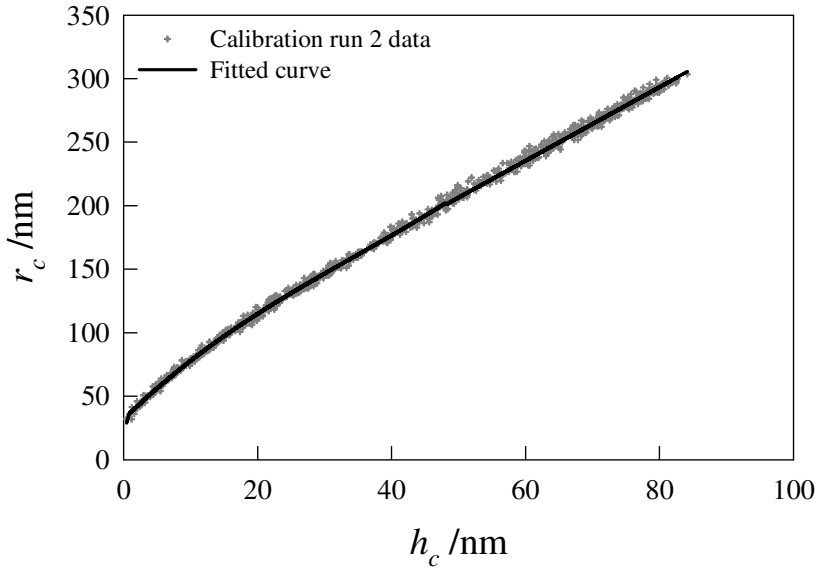

Figure 4. a) Comparison of all 3 calibrations and b) a fit of $r_c = ah_c + bh_c^{1/2} + c$ over the lowest depth region combined fit with a straight line fit at greater depths for calibration run 3.

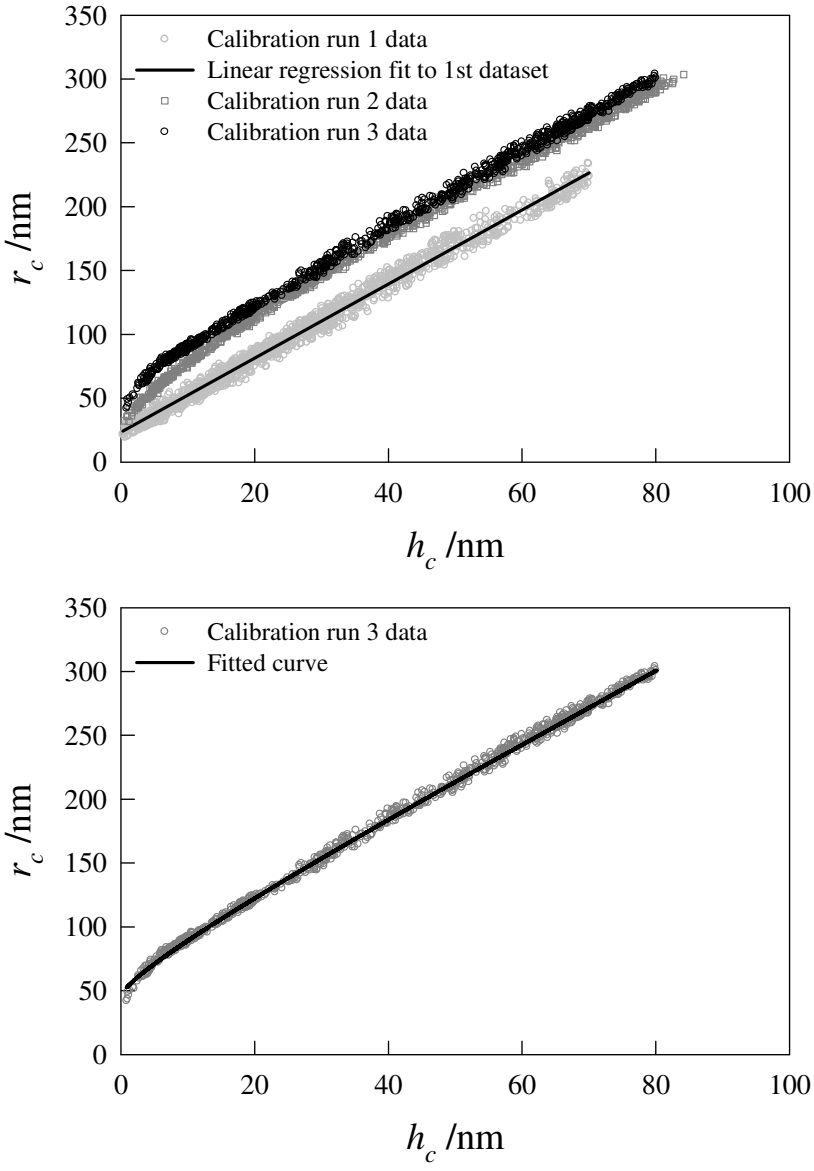

Figure 5. Residuals from the fits to all 3 calibration runs a) obtained by fitting to $r_c$ and b) obtained from the Oliver and Pharr fit but plotted in terms of $r_c$ for comparative purposes

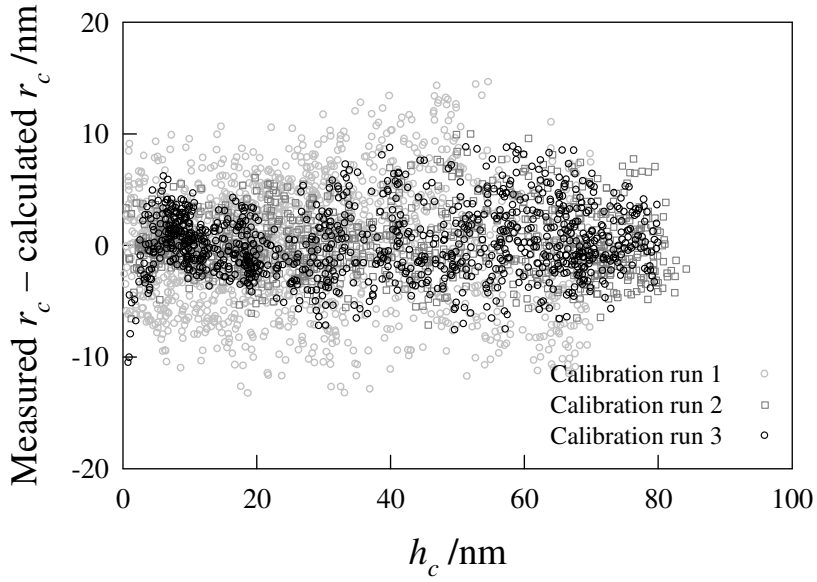


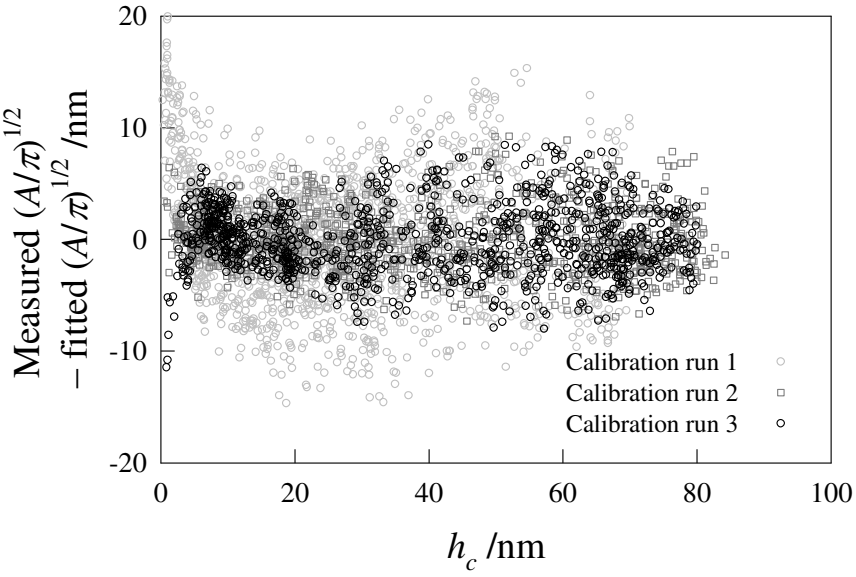

Figure 6. a) Reduced modulus and b) hardness plots obtained using calibration equations (7), (11) and (12).

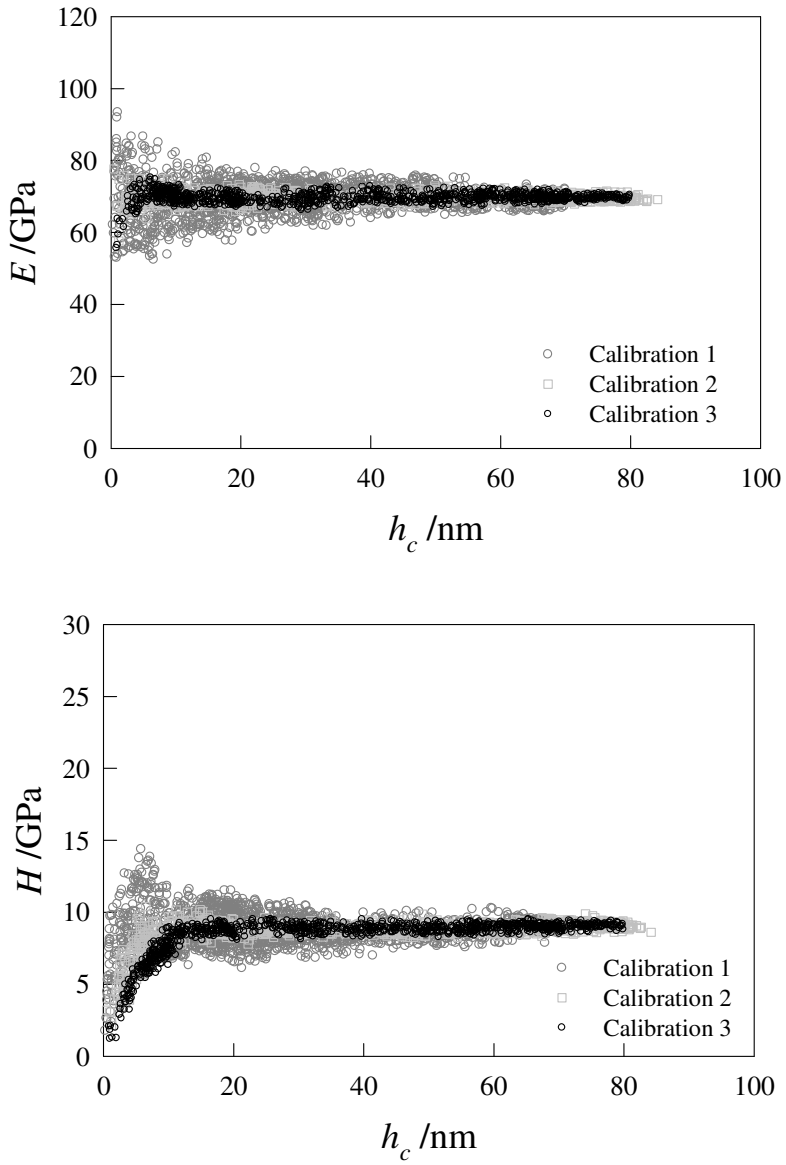

Figure 7. a) Reduced modulus and b) hardness plots obtained using 9 term Oliver and Pharr TAF type fits.